Fundamental insight into pyrolysis and oxidation process of ferric (III) stearate

Almaz L. Zinnatullin [a], Chengdong Yuan [b,c,*], Dmitrii A. Emelianov [c], Mikhail A. Varfolomeev [b,c,*], Farit G. Vagizov [a,**]

[a] Institute of Physics, Kazan Federal University, Kazan 420008, Russia
[b] Department of Petroleum Engineering, Kazan Federal University, Kazan 420008, Russia
[c] Department of Physical Chemistry, Kazan Federal University, Kazan 420008, Russia

ARTICLE INFO

ABSTRACT

Recently, metal organic complexes have attracted a lot of attention as oil-dispersed catalysts for in-situ combustion and upgrading of heavy oil. As a relatively new topic, their catalytic mechanism has not been clearly understood. The pyrolysis and oxidation process of metal organic complexes is very important for their catalytic function. In this work, we investigated the pyrolysis and oxidation process of ferric(III) stearate by thermogravimetric analysis (TGA), X-ray diffraction (XRD), and Mössbauer spectroscopy analysis. The results indicated that the pyrolysis and oxidation of ferric(III) stearate is a multistage process. Isothermal treatments experiments show that ferric(III) stearate begins to decompose at about 200 °C and produce ferrous(II) stearate. From 200 to 300 °C, there are three processes that may occur simultaneously: ferric(III) stearate → ferrous(II) stearate; ferrous (II) stearate → Fe_3O_4; and ferric(III) stearate → Fe_3O_4. At 300–350 °C, iron(II) oxide (FeO) is formed with a complete decomposition of ferric(III) stearate. A further heating up to 500 °C leads to the oxidation of FeO to Fe_3O_4, and Fe_3O_4 is the final solid-state product. The degradation kinetics of ferric(III) stearate were analyzed by both isoconversional model and reaction-order model. For reaction-order model, five contributions with the activation energy values in the range of 110–250 kJ/mol were identified and compared with isothermal experiments results. The findings in this work are of great value for understanding the catalytic mechanism of ferric (III) stearate as oil-dispersed catalysts for in-situ catalytic upgrading of heavy oil as well as in-situ combustion for heavy oil recovery.

1. Introduction

Transition-metal organic complexes have been used as catalysts in different topics, such as environmental remediation (water treatment) [1] and oxidation of organic compounds [2,3]. Recently, there is a strong interest in applying transition-metal organic complexes as catalysts in heavy oil upgrading and recovery processes. As is well known, heavy oil, extra-heavy oil, and bitumen have a proportion of about 60–70% of the total world's oil reserves. Unlike conventional light oils, these heavy crudes have high density and viscosity, which causes a lot of issues for their development. Generally, thermal methods, mostly steam injection and in-situ combustion techniques, are used to effectively develop heavy oils. To improve the efficiency of steam injection and in-situ combustion for heavy oil recovery, catalysts are being applied in

these thermal processes. For steam injection, catalysts are utilized to promote aquathermolysis (main reaction in steam injection process) to achieve a high level in-situ upgrading of heavy oils as well as to reduce fresh water and energy used to generate steam. For in-situ combustion process, catalysts are utilized to enhance the combustion efficiency of heavy oils combining with in-situ oil upgrading. Recently, transition-metal organic complexes have been proved to have a high potential as catalysts for these two processes. The catalytic mechanism of these transition-metal organic complexes has been found to be associated with their pyrolysis and oxidation process where active phases (usually metal and metal oxide nanoparticles) are in-situ generated during the cracking and/or oxidation process of heavy oils. For instance, in our recent work, we found that the pyrolysis and oxidation of copper stearate in heavy oil combustion process in-situ generated Cu, Cu_2O, and
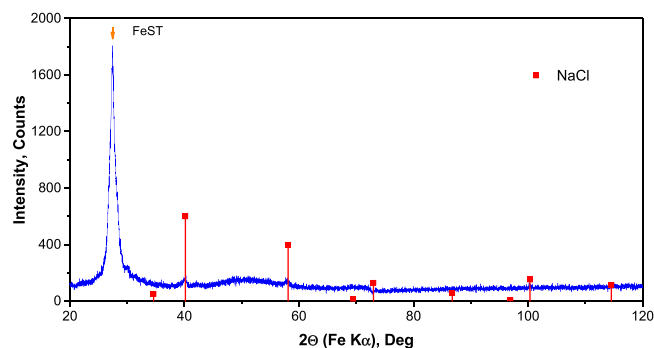

Fig. 1. XRD pattern of initial ferric(III) stearate.

CuO nanoparticles as catalysts.

As indicated by recent studies, nanoparticles have sprung up as effective catalysts for heavy oil recovery and in-situ upgrading nowadays [4]. However, the direct application of these nanoparticle catalysts for these purposes are being faced with a lot of challenges. For instance, the transportation of nanoparticles in porous media to the targeted zone in reservoir is difficult due to high retention, aggregation, deposition, and possible pore blocking [4–6]. In addition, these nanoparticles must keep a highly dispersed state in oil environment to give a high catalytic activity, which is difficult without an additional aid. The advantage of using transition-metal organic complexes is that they can be easily dispersed in oil environment for easy transportation and keep a highly dispersed state because of their oil-dispersing property. In our recent work, we compared the catalytic effect of CuO nanoparticles and copper stearate for heavy oil oxidation [5]. Copper stearate displayed a much better catalytic performance. CuO nanoparticles were in-situ generated and evenly distributed in oil environment, which plays a vital role in enhancing their catalytic efficiency.

However, for the selection of suitable metal organic complexes for different reactions (such as aquathermolysis reactions and oxidation reaction) at various treatment temperatures, it is indispensable to study the pyrolysis and oxidation process of these metal organic complexes to understand at which temperature what kind of active phases can be formed to be as catalysts. Iron compounds with various oxidation states and structures from metallic iron to ferric oxides, exhibit many unique properties, making them be widely used as catalysts [7–9]. Different iron oxides have been tested for in-situ upgrading and combustion [10–14]. In this work, we will focus on understanding the mechanism of the pyrolysis and oxidation process of ferric(III) stearate considering that iron oxide nanoparticle is one of the most popular catalysts due to its many years' application and low cost as well as the proved catalytic effect of ferric(III) stearate in in-situ upgrading and combustion of heavy oil [5,15].

It should be noticed that the thermal decomposition of metal carboxylates has also been used as a low-cost and simple method to synthesize metal oxide nanoparticles. The oxidation state of nanoparticles as well as their shape and size can be precisely controlled by external conditions, namely, atmosphere, organic ligands, temperature, and time of treatment [16–20]. Another advantage of this method is that the synthesis of nanoparticles can be carried out at relatively low pyrolysis temperatures and in a continuous mode [21]. It was shown earlier that almost uniform nanoparticles of transition metal oxides were produced by the thermal decomposition of carboxylates of these metals [21–23]. The results obtained from these reports to some extent support that the in-situ generation of metal nanoparticles as catalysts is a promising method for in-situ oil upgrading and combustion for heavy oil recovery.

In fact, the thermal decomposition of metallic carboxylates is a complex process [24]. The reactions leading to the formation of oxides are still not fully understood, even though several reaction pathways for the decomposition of carboxylates have been proposed [20]. Therefore,

an important task is to determine the reaction products at each stage of the decomposition of metallic carboxylates. Mössbauer spectroscopy can play an important role in understanding the thermal decomposition of iron carboxylates because it can determine the valence state and features of the local environment of resonant atoms (Fe as well as Sn, Eu) in any condensed media, including amorphous. In addition, Mössbauer measurements allow one to obtain some important characteristics of solids, for instance, Debye temperature [25]. In early time, Mössbauer spectroscopy was applied to study the decomposition of potassium tris(malonate) ferrate(III) trihydrate [26], iron(III) propionate trihydrate ($Fe(C_3H_5O_2)_3 \cdot 3H_2O$) and iron(III) butyrate trihydrate ($Fe(C_4H_7O_2)_3 \cdot 3H_2O$) [27], Fe(II) malonate dihydrate and Fe(II) formate dihydrate [28], iron(III) lactate ($Fe(CH_3CHOHCOO)_3$), iron(III) tartrate ($Fe_2(C_4H_4O_6)_3$), and iron(III) citrate ($Fe(C_6H_5O_7) \cdot 5H_2O$) [29].

In this work, to our knowledge, for the first time the complex thermal decomposition processes (pyrolysis and oxidation) of ferric(III) stearate were investigated up to 500 °C in an air atmosphere. A deep understanding of decomposition/oxidation kinetics of ferric(III) stearate is not only valuable for understanding the catalytic mechanism of as oil-dispersed catalysts for in-situ catalytic upgrading of heavy oil as well as in-situ combustion processes for heavy oil recovery, but also can provide additional fundamental knowledge for the synthesis of metal oxide nanoparticles since thermal decomposition of metal carboxylates has been used as a low-cost and simple method to controllably synthesize metal oxide nanoparticles. Furthermore, we present a detailed Mössbauer spectroscopy analysis of ferric(III) stearate in the temperature range of 80–300 K. Based on the improved Debye model, effective Debye temperatures are reported both for ferric and ferrous stearates.

2. Experimental section

Ferric(III) stearate with the purity of 98% was purchased from Shanghai Macklin Biochemical Co., Ltd. (China). Isothermal pyrolysis and oxidation experiments of ferric(III) stearate were conducted at various temperatures in open flask in air atmosphere for 2 h. Solid residues after the pyrolysis and oxidation were investigated by X-Ray diffraction (XRD) and Mössbauer spectroscopy. For XRD studies, *MD-10* desktop diffractometer (*Radicon*, Russia) with Fe-Kα radiation tube (λ = 0.193728 nm) was used. The diffractometer worked in the Debye-Scherer geometry and the angular accuracy was about ± 0.02° for the position of the reflex. XRD patterns were recorded in the 2θ range of 20°–120° with the step of 0.015° at room temperature. The Mössbauer effect studies were conducted on conventional *WissEl* Gmbh (Germany) spectrometer operating in a constant acceleration mode. The studies were provided in transmission geometry. Commercial ^{57}Co(Rh) Mössbauer source with about 40 mCi activity was used as resonant γ-radiation source. Mössbauer spectra were collected within the temperature range of from −193 °C (80 K) to room temperature. Low-temperature measurements were carried out with a continuous flow cryostat (model *CFICEV* from *ICE Oxford*, UK) equipped with CryoCon 32B temperature controller. The spectrum of thin metallic iron foil was used for the calibration of the spectrometer velocity scale. The experimental data were processed by the least-square method using *SpectrRelax* software [30]. The isomer shifts values were given relative to the α-Fe spectrum center at room temperature. Thermal analysis methods, such as thermogravimetric analysis (TGA) and differential scanning calorimeter (DSC), have been widely used for characterizing the pyrolysis and oxidation process of organic materials [31–33]. In this work, TGA test for studying the pyrolysis and oxidation process of ferric(III) stearate at elevated temperature was performed in a *NETZSCH TG 209 F1 Libra* analyzer under air atmosphere. Temperature was elevated from 30 to 850 °C at multiple heating rates (4, 6, 8, and 10 °C /min). The sample mass was about 50 mg. The experiments were performed twice for reproducibility. The reproducibility was good with a standard error of ± 0.5 °C for the same conversion rate. Prior to measurements, the calibration of thermocouple was performed. A detailed description of

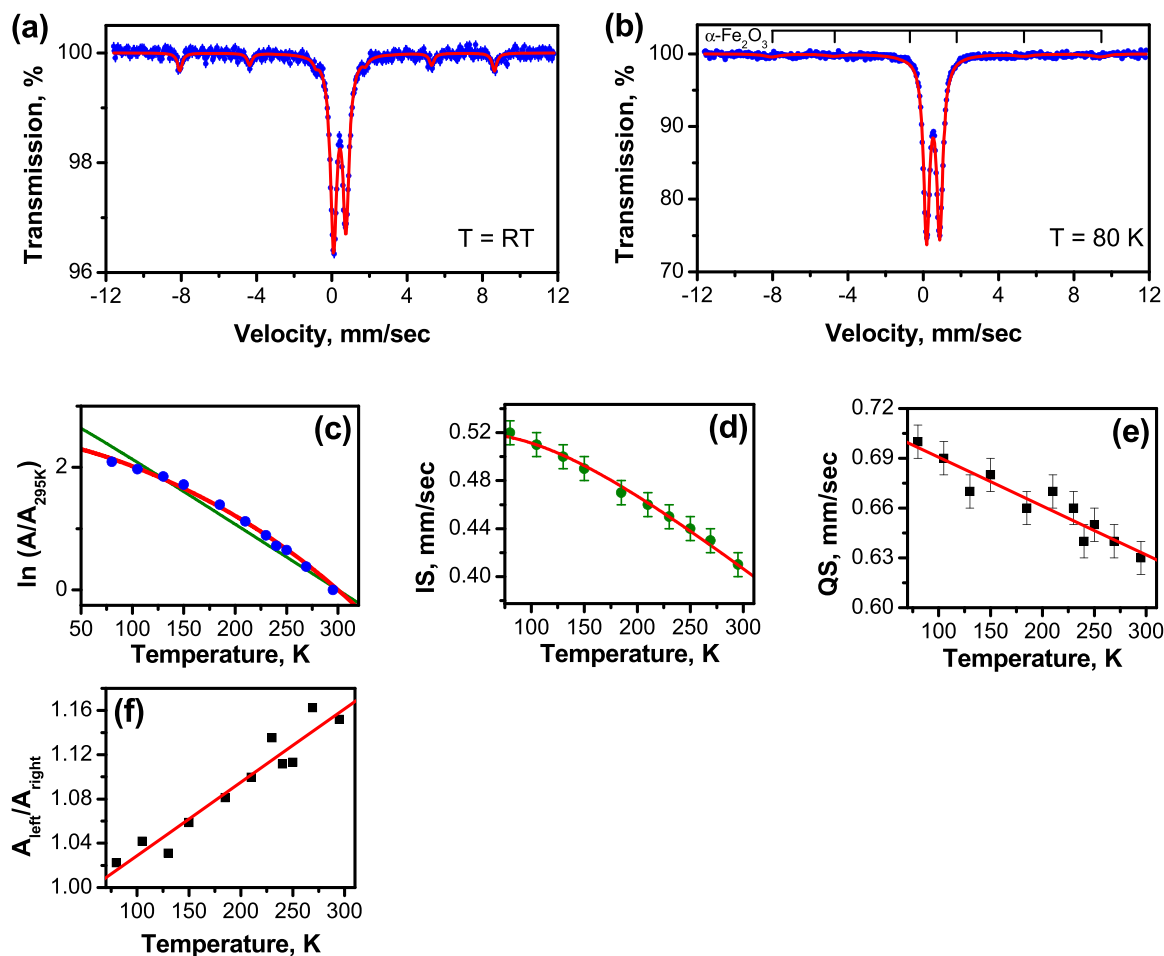**Fig. 2.** Mössbauer spectra of ferric(III) stearate sample recorded at room temperature (a) and 80 K (−193 °C) (b); the temperature dependencies of the hyperfine parameters of the doublet assigned to ferric(III) stearate: Mössbauer absorption area (c), isomer shift IS (d), quadrupole splitting QS (e), and asymmetry of doublet (f).

TGA experiments can be found in our previous work [34].

3. Results and discussion

XRD pattern of initial ferric(III) stearate is shown in Fig. 1. There are a number of reflexes. One of them marked with orange arrow is associated with ferric(III) stearate. This reflex located at 2θ = 27.4° which corresponds to a D-space of 0.41 nm. The reflex is wide enough and commonly related with amorphous stearate phase [35]. Other reflexes marked with red squares are associated with sodium chloride (NaCl) which exists as impurity.

Mössbauer spectra recorded at room temperature and 80 K (−193 °C) are shown in Fig. 2a and b, respectively. Room temperature Mössbauer spectrum was processed by two components, namely, sextet (isomer shift (IS) = 0.41 ± 0.02 mm/s, quadrupole splitting (QS) = −0.22 ± 0.02 mm/s, hyperfine magnetic field (HF) = 514 ± 1 kOe) and asymmetrical quadrupole doublet (IS = 0.41 ± 0.01 mm/s, QS = 0.63 ± 0.01 mm/s). The sextet was assigned to hematite (α-Fe$_2$O$_3$). The second component has the parameters that are the characteristics of ferric ions and close to values reported earlier for ferric(III) stearate [36]. Therefore, the doublet should associate with ferric(III) stearate phase.

The temperature dependencies of the doublet parameters are shown in Fig. 2c and d. With the decrease of temperature, a strong influence of absorption area was observed (Fig. 2c). The area of the Mössbauer spectrum is proportional to the probability of recoilless processes, i.e. the Lamb–Mössbauer factor (recoil free fraction):

$$A \sim f \tag{1}$$

$$f = e^{-k^2 \langle x^2 \rangle} \tag{2}$$

where $\langle x^2 \rangle$ – mean-square displacement, and k – wavenumber of resonant γ-photon [37]. In the approximation of Debye model, it can be written as:

$$\ln f = -\frac{3E_R}{2k_B\theta_D}\left[1 + 4\left(\frac{T}{\theta_D}\right)^2 \int_0^{\theta_D/T} \frac{x\,dx}{e^x - 1}\right] \tag{3}$$

where θ_D – Debye temperature, k_B – Boltzmann constant, $E_R = \frac{E_\gamma}{2Mc^2}$ – recoil energy of atom with mass of M, E_γ – energy of γ-photon, and c – light velocity. The temperature dependence of the normalized area is determined by the following expression:
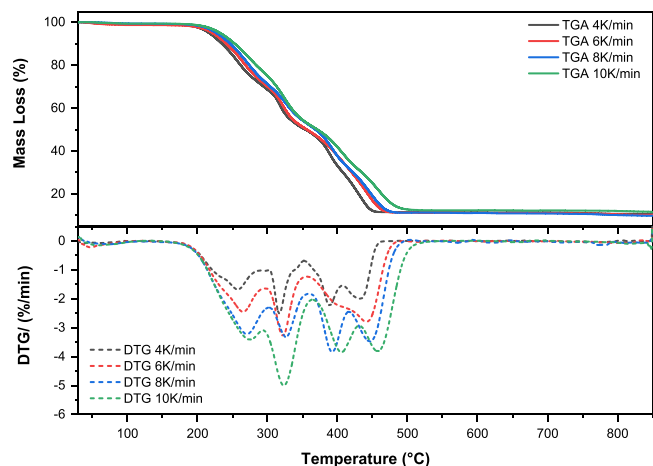
Fig. 3. TG-DTG curves for the pyrolysis and oxidation of ferric(III) stearate.

$$\langle v^2 \rangle = \frac{9k_B\theta_D}{M}\left[\frac{1}{8} + \left(\frac{T}{\theta_D}\right)^4\int_0^{\frac{\theta_D}{T}}\frac{x^3}{e^x-1}dx\right]. \tag{9}$$

The experimental temperature dependence of isomer shift was mathematically processed by following expression:

$$\delta = \delta_S - \frac{9k_B\theta_D}{2cM}\left[\frac{1}{8} + \left(\frac{T}{\theta_D}\right)^4\int_0^{\frac{\theta_D}{T}}\frac{x^3}{e^x-1}dx\right] \tag{10}$$

The experimental data and fitted curve are shown in Fig. 2d by red line. Best fit parameters are $\theta_D = 485 \pm 21$ K and $\delta_s = 0.65 \pm 0.01$ mm/ s.

Debye temperature estimated from the temperature dependence of isomer shift is almost four time higher than the one derived from the temperature dependence of Mössbauer absorption area. This discrepancy can be explained if we consider the fact that the Lamb–Mössbauer factor (recoil free fraction) is determined by the mean square displacement, while the second-order Doppler shift is determined by the mean

$$\ln\frac{A(T)}{A(295\ K)} = \ln\frac{f(T)}{f(295\ K)} = \frac{6E_R}{k_B\theta_D}\left[\left(\frac{295\ K}{\theta_D}\right)^2\int_0^{\frac{\theta_D}{295\ K}}\frac{x}{e^x-1}dx - \left(\frac{T}{\theta_D}\right)^2\int_0^{\frac{\theta_D}{T}}\frac{x}{e^x-1}dx\right] \tag{4}$$

However, the mathematical least-square processing of experimental Mössbauer area data by Eq. (4) does not give a satisfactory result (green curve on Fig. 2c). One of reasons may be the anharmonicity of the vibrations of resonant atoms relative to their equilibrium positions. Commonly, the displacement of atoms is the sum of some contributions which are statistically independent. According to Frauenfelder et al. [38], mean square displacement can be written as following sum:

$$\langle x^2 \rangle = \langle x_v^2 \rangle + \langle x_c^2 \rangle + \langle x_d^2 \rangle \tag{5}$$

where $\langle x_v^2 \rangle$, $\langle x_c^2 \rangle$, $\langle x_d^2 \rangle$ are the lattice vibration contributions, the conformation contributions, and the diffusion contributions, respectively. In the simplest case, we can take anharmonicity into account by introducing a temperature dependence of Debye temperature in the limit of linear approximation [39]:

$$\theta_D(T) = \theta_D(0)\cdot(1 + A\cdot T + ...) \tag{6}$$

where $\theta_D(0)$ – Debye temperature at 0 K, A – anharmonicity parameter, and T – temperature. The experimental data were processed using expression (4), which considers the linear dependence (6) of Debye parameter, θ_D, on temperature. The fitting result is shown in Fig. 2c by a red line. The following parameters were obtained: $\theta_D(0) = 125 \pm 2$ К и and $A = -0.096 \pm 0.011$ K^{-1}.

The isomer shift is determined by sum of two contributions, δ_s and δ_{SOD}, which are related to the density of s electrons on nuclei and the second order Doppler shift, respectively:

$$\delta = \delta_s + \delta_{SOD} \tag{7}$$

In many cases, the temperature dependence of δ_s is negligible. Temperature dependence of isomer shift commonly is defined by the second order Doppler shift:

$$\delta_{SOD} = -\frac{\langle v^2 \rangle}{2c} \tag{8}$$

where $\langle v^2 \rangle$ – the mean square velocity of resonance atoms. In the Debye approximation, it can be written as:

square velocity of resonant atoms. Mean square displacement depends on low-frequency vibrations up to 250 cm^{-1}, whereas mean square velocity depends on higher frequency vibrations in the range of 400–800 cm^{-1} [40]. The intermolecular vibrations of ferric(III) stearate molecules are characterized by low frequencies because of the heavy mass of the molecules and a relative weak bond between them. In contrast, the intramolecular vibrations of Fe atoms in the molecule expand to higher frequencies. Thus, intermolecular vibrations have contribution mainly to the mean square displacement, while intramolecular vibrations contribute to both the mean square displacement and the mean square velocity [41].

With increasing temperature, a slight decrease in the quadrupole splitting is observed (Fig. 2e). Generally, quadrupole splitting is defined by the interaction between electric field gradient (EFG) and nuclear quadrupole moment. There are two main contributions in EFG, namely, the contribution of valence electrons and the lattice contribution [37]. The former is strongly temperature-dependent, while the latter is weakly dependent on temperature. However, in the case of the high-spin Fe^{3+}, considering a crystal field model with no overlap of ligand and metal orbitals, valence electron contribution may be neglected since half-filled *3d* orbitals of this ion results in a spherical symmetry of electron distribution [37]. Thus, the observed slight decrease in quadrupole splitting value with temperature increase arises from lattice contribution to EFG. Doublet asymmetry, which is defined here as the ratio of the area of the left resonance line to the area of the right line, increases with temperature (Fig. 2f). However, the widths of these lines are equal in the whole investigated temperature range. Such behavior is often associated with the Gol'danskii–Karyagin effect [42,43]. This effect may be caused by the difference of chemical bonding in different directions [44].

Fig. 3 shows the pyrolysis and oxidation behavior of ferric(III) stearate obtained from TGA experiments. Four noticeable processes can be observed during the heating process in air. Temperature and mass loss data for each process are presented in Table 1. For determining the reaction mechanism of each process, isothermal treatments were conducted at different temperatures. Solid products obtained from these treatments were *ex-situ* investigated by XRD and Mössbauer

Table 1
Temperature data and mass loss of each process observed in TG-DTG curves.

| Heating rate (K/min)	Process 1			Process 2			Process 3			Process 4		
	Temperature range (°C)	Peak (°C)	Mass loss (%)	Temperature range (°C)	Peak (°C)	Mass loss (%)	Temperature range (°C)	Peak (°C)	Mass loss (%)	Temperature range (°C)	Peak (°C)	Mass loss (%)
4	150–296	257.6	29.37	296–352	316.9	19.30	352–407	389.4	20.17	407–500	433.4	18.84
6	150–297	264.8	27.94	297–356	321.8	20.68	356–406	398.0	14.44	406–520	439.3	24.40
8	150–303	270.5	29.03	303–360	326.6	18.33	360–418	392.5	20.59	418–525	446.4	20.17
10	150–294	274.8	22.64	294–365	323.4	25.45	365–431	405.1	20.19	431–540	457.8	18.75
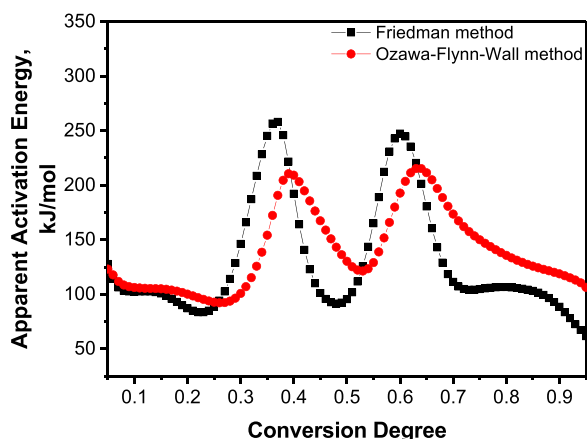
Fig. 4. Apparent activation energy dependence on conversion degree derived by Friedman and Ozawa–Flynn–Wall methods.
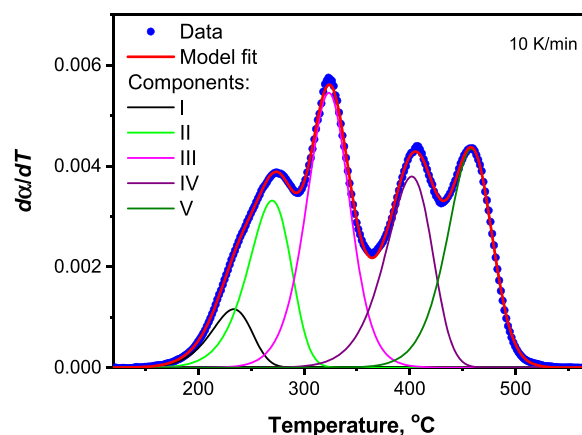

Fig. 6. Model multi-step fitting of the first derivative of conversion degree data taken in TGA experiment with the heating rate of 10 K/min.
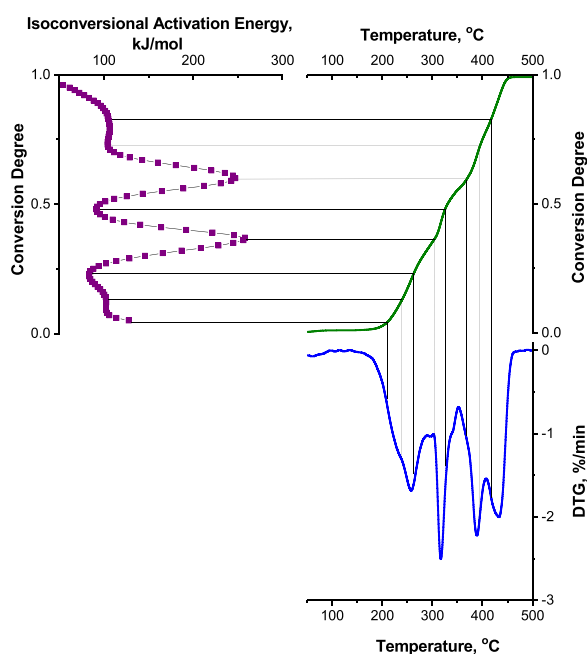

Fig. 5. Merged data of Friedman isoconversional analysis and TGA-DTG curves (4 K/min).

spectroscopy. It should be mentioned that in-situ studies of thermal treatment of ferric(III) stearate are almost practically impossible to obtain useful information due to low Debye temperature that leads to an almost absence of Mössbauer effect at high temperatures.

The data of TGA were also analyzed by differential (Friedman method) and integral (Ozawa–Flynn–Wall) isoconversional methods to estimate kinetics. These methods were described elsewhere [45–47].

The kinetic analysis results are depicted in Fig. 4. It is seen that with a rise of conversion degree, apparent activation energy drastically changes in the range from 50 to 270 kJ/mol. Such changes are another proof of the multistep decomposition process of ferric(III) stearate. To better understand the process, the results of isoconversional analysis by Friedman method and TG-DTG curves (4 K/min) are merged in Fig. 5. Some "special" points on apparent activation energy fingerprint are projected on TG-DTG data. Obviously, these points are in concordance with the steps of thermal pyrolysis and oxidation of ferric(III) stearate.

Furthermore, the TGA data were processed based on the model expressions proposed by Coats and Redfern [48]. In general, kinetics of chemical reaction is described by rate expression (11):

$$\frac{d\alpha}{dt} = k \cdot f(\alpha) \tag{11}$$

where α – conversion degree, k – rate coefficient, $f(\alpha)$ – conversion function, and t – time. Conversion degree is determined using Eq. (12):

$$\alpha = \frac{m_0 - m}{m_0 - m_\infty} \tag{12}$$

where m – mass at given time, and m_0 and m_∞ – starting and final masses, respectively. Conversion degree changes in the range from 0 to 1. Rate coefficient k is described by Arrhenius law:

$$k = A e^{\frac{-E_a}{RT}} \tag{13}$$

where A – preexponential Arrhenius factor, E_a – apparent activation energy, R – the ideal gas constant, and T – absolute temperature. There are a lot of conversion functions being used for describing various processes [49]. Here, we will use the simplest form of $f(\alpha)$ denoted as reaction order-model:

$$f(\alpha) = (1 - \alpha)^n \tag{14}$$

where n – reaction order.

Table 2
Values of parameters taken from mathematical processing of TGA data (10 K/min).

Kinetic parameters	Component I	Component II	Component III	Component IV	Component V
E_a, kJ/mol	115.8 ± 0.6	125 ± 5	183 ± 2	182.3 ± 0.7	247 ± 1
A, s^{-1}	$8.3 \pm 1.5 \times 10^9$	$1.1 \pm 0.7 \times 10^{10}$	$1.4 \pm 0.5 \times 10^{14}$	$1.1 \pm 0.2 \times 10^{12}$	$4.7 \pm 0.9 \times 10^{15}$
n	1.15 ± 0.04	1.13 ± 0.04	1.61 ± 0.01	1.15 ± 0.01	1.37 ± 0.01
w	0.05 ± 0.01	0.18 ± 0.01	0.293 ± 0.001	0.218 ± 0.001	0.240 ± 0.001
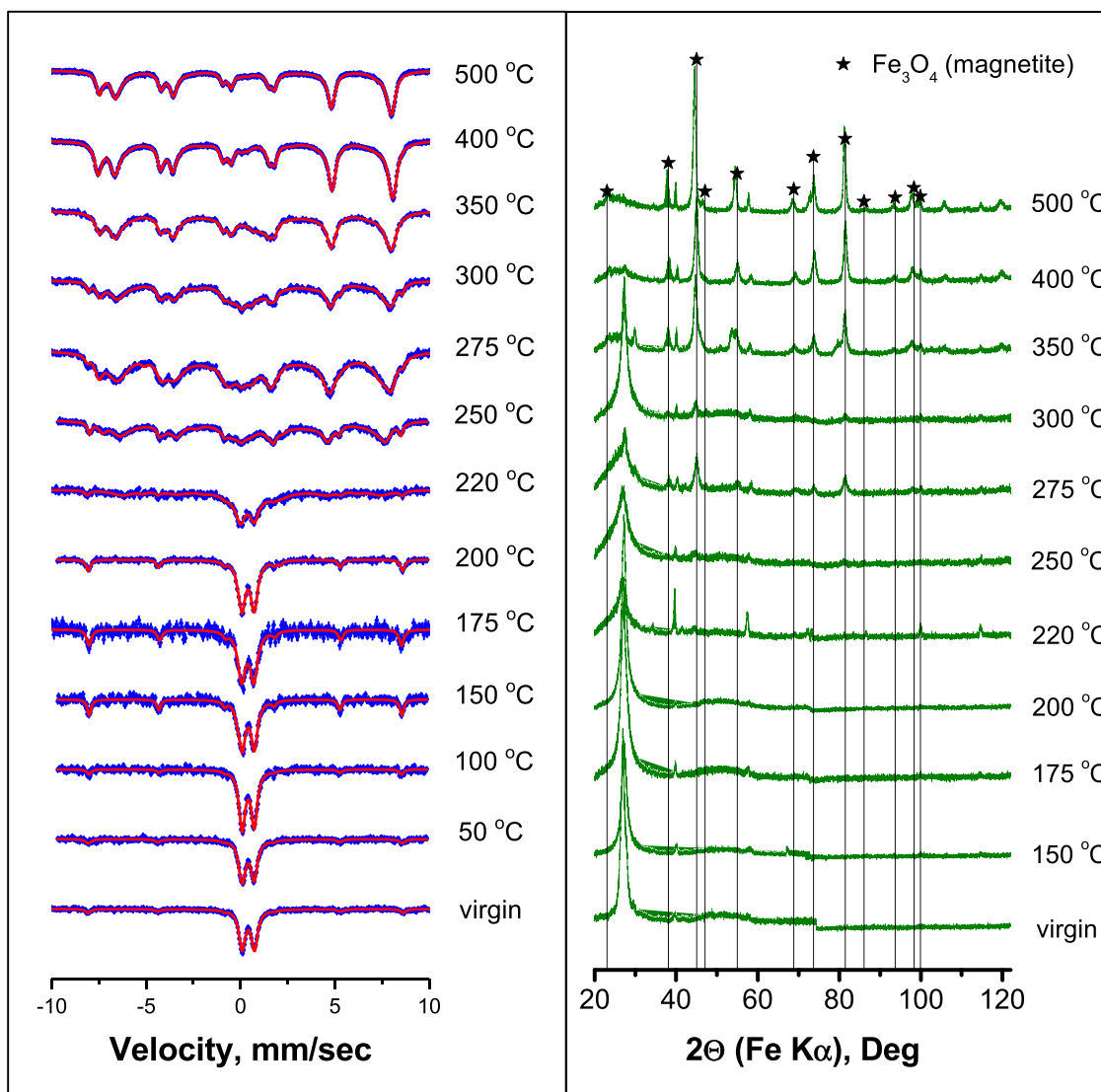
Fig. 7. Mössbauer spectra (left) and XRD patterns (right) of ferric(III) stearate after isothermal treatment at different temperatures.

Typically, TGA experiments were performed at a specific heating rate:

$$\beta = \frac{dT}{dt} \qquad (15)$$

Finally, the following model chemical kinetics expression can be obtained:

$$\frac{d\alpha}{dT} = \frac{A}{\beta} e^{\frac{-E_a}{RT}} \cdot (1-\alpha)^n \qquad (16)$$

Further, this expression is integrated as described by Jasinki [48]:

$$\text{for n} = 1: \; -\ln\left(1-\alpha\right) = \frac{ART^2}{\beta E_a}\left[1-\frac{2RT}{E_a}\right]e^{-\frac{E_a}{RT}} \qquad (17)$$

$$\text{for n} \neq 1: \; \frac{1-(1-\alpha)^{1-n}}{1-n} = \frac{ART^2}{\beta E_a}\left[1-\frac{2RT}{E_a}\right]e^{-\frac{E_a}{RT}} \qquad (18)$$

After simple manipulations:

$$\text{for n} = 1: \; \alpha = 1 - \exp\left[\frac{ART^2}{\beta E_a}\left[1-\frac{2RT}{E_a}\right]e^{-\frac{E_a}{RT}}\right] \qquad (19)$$

$$\text{for n} \neq 1: \; \alpha = 1 - \left[1-\left(1-n\right)\frac{ART^2}{\beta E_a}\left[1-\frac{2RT}{E_a}\right]e^{-\frac{E_a}{RT}}\right]^{\frac{1}{1-n}} \qquad (20)$$
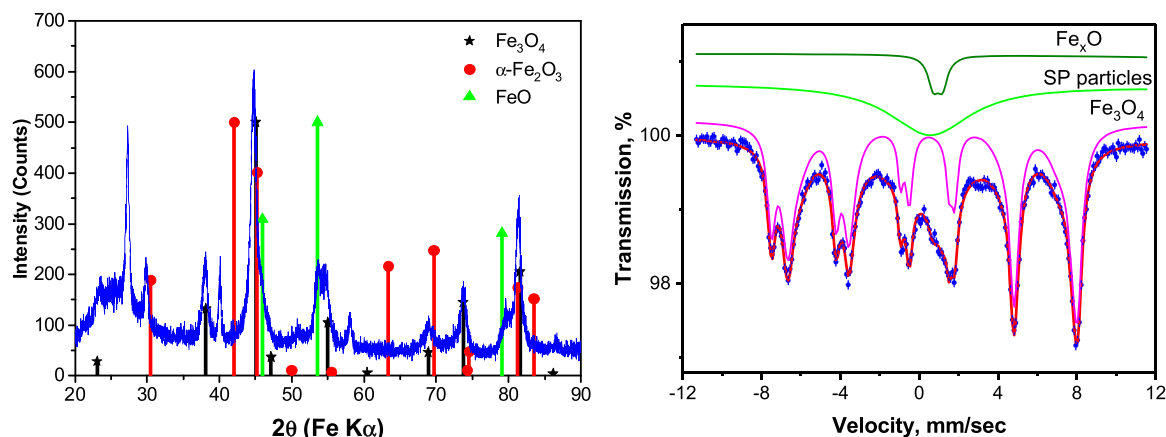
Fig. 8. XRD pattern (left) and room temperature Mössbauer spectrum (right) of ferric(III) stearate after treatment at 350 °C.
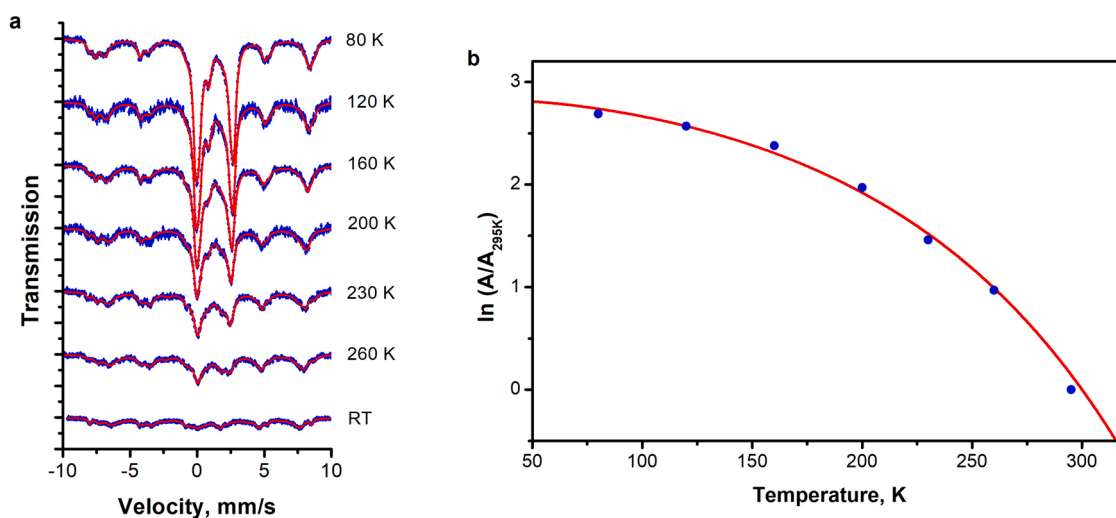

Fig. 9. Mössbauer spectra of ferric(III) stearate after treatment at 250 °C recorded at various temperatures (a); temperature dependence of the relative area of doublet related to ferrous(III) stearate (b).

Table 3
Debye temperatures and values of Lamb–Mössbauer factor at room temperature for iron containing phases.

Phase		Debye temperature, K	Lamb–Mössbauer factor at room temperature, f_{295K}	Source
Ferric(III) stearate		125	0.01	This study
Ferrous(II) stearate		117	0.0002	This study
α-Fe$_2$O$_3$		~ 500	0.84	De Grave and Vandenberghe [54]
Fe$_3$O$_4$	Oct	314	0.66	Sawatzky et al. [55]
	Tetr	334	0.69	
Fe$_x$O		430	0.8	Stolen et al. [56]

After differentiation with respect to T and simple rearrangement:

$$\text{for } n = 1 : \frac{d\alpha}{dT} = \frac{A}{\beta}\left[1 - \frac{6R^2T^2}{E_a^2}\right]\exp\left[-\frac{E_a}{RT} + \frac{ART^2}{\beta E_a}\left(1 - \frac{2RT}{E_a}\right)e^{-\frac{E_a}{RT}}\right] \quad (21)$$

$$\text{for } n \neq 1 : \frac{d\alpha}{dT} = \frac{A}{\beta}\left[1 - \frac{6R^2T^2}{E_a^2}\right]e^{-\frac{E_a}{RT}}\left[1 - (1-n)\frac{ART^2}{\beta E_a}\left(1 - \frac{2RT}{E_a}\right)e^{-\frac{E_a}{RT}}\right]^{\frac{n}{n-1}} \quad (22)$$

Expressions (19)–(22) may be used for the analysis of single-step thermal conversion. However, often conversion is multi-step process. In such cases, experimental data can be processed by the sum of contributions:

$$\frac{d\alpha}{dT} = \sum_{i=1}^{l} w_i \frac{d}{dT}\alpha\left(A^i, E_a^{\,i}, n^i\right) \quad (23)$$

where w_i – weight of i-th contribution and l – number of contributions. Each of these contributions is related to one kinetic process, and kinetic parameters (A, E_a, n) are determined for each component.

TGA data were processed by expression (23). The data at 10 K/min and its fitting curve are presented in Fig. 6. These data were processed by the sum of five components, and the estimated parameters of these components are listed in Table 2. It can be seen that the estimated values of apparent activation energy for each process (100–250 kJ/mol) are in the main range of values calculated by isoconversional methods (Fig. 4). The division of these processes can provide a basis for understanding the pyrolysis and oxidation process of ferric(III) stearate.

Room temperature Mössbauer spectra and XRD patterns of ferric(III) stearate after isothermal treatment at different temperatures are depicted in Fig. 7. It is clearly seen that thermal treatment has a strong influence on the phase composition of the system. When temperature is < 200 °C, XRD patterns as well as Mössbauer spectra of samples are almost the same for each temperature. Thus, during annealing at these
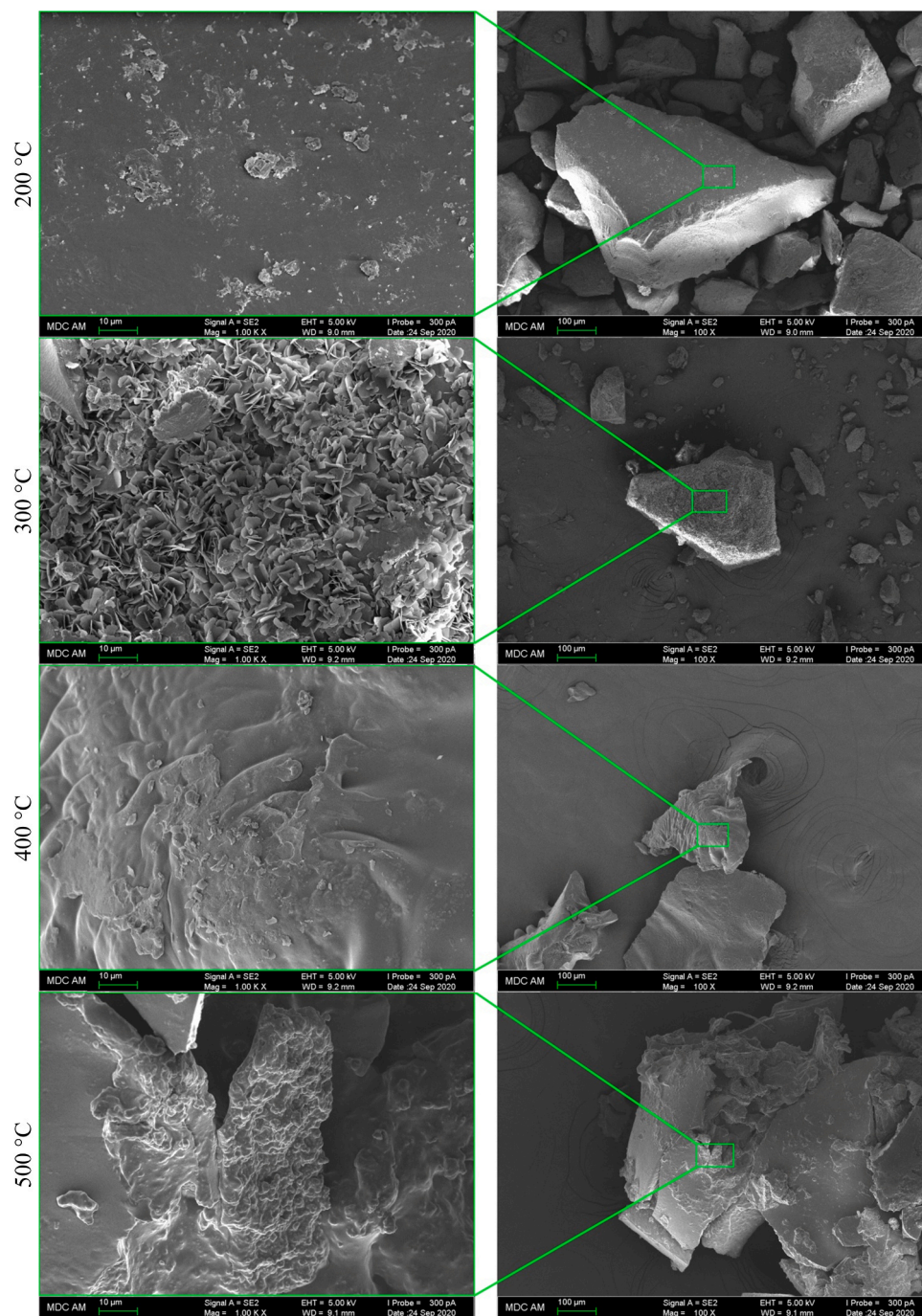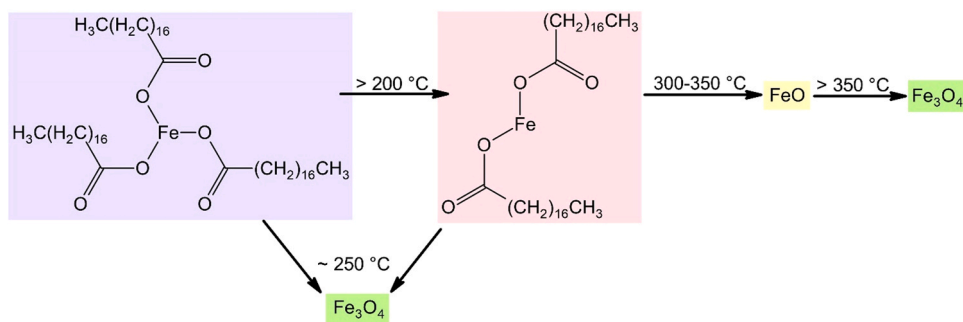
Fig. 10. SEM images of ferric(III) stearate calcined at 200 °C, 300 °C, 400 °C, and 500 °C (from top to bottom).

Scheme 1. Pathway of the pyrolysis and oxidation of ferric(III) stearate in air atmosphere.

temperatures the phase composition of obtained products does not change qualitatively. However, the relative area of sextet related to hematite in Mössbauer spectra increases with temperature. This is a sign that ferric(III) stearate is slowly decomposed with the formation of hematite in the range of ~ 100–200 °C. At the temperatures above 200 °C, new components, namely, a doublet and two sextets, appear in the Mössbauer spectra in addition to abovementioned lines. Hyperfine parameters of the "new" doublet (at room temperature: IS = 0.97 ± 0.01 mm/s, QS = 2.27 ± 0.01 mm/s) are the characteristics of ferrous(II) ions. Two sextets with the following hyperfine parameters: IS = 0.27 ± 0.01 mm/s, QS = 0 ± 0.01 mm/s, HF = 480 ± 1 kOe and IS = 0.56 ± 0.01 mm/s, QS = 0 ± 0.01 mm/s, HF = 437 ± 1 kOe, are corresponding to iron ions in tetrahedral and octahedral cites of magnetite (Fe_3O_4) phase, respectively. At 250 °C and above, an abrupt increase of magnetite content is observed. XRD investigations confirm Mössbauer spectroscopy results. Actually, the decrease of the intensity of ferric(III) stearate reflex and appearance of new reflexes linked to magnetite starts at 200 °C and are intensified at higher temperatures. Magnetite reflexes (shown by black asterisks on Fig. 7) noticeably increase after the thermal treatment at 250 °C and above. After treatment at 350 °C, hematite lines disappear in Mössbauer spectrum. It means that full or partial reduction of ferric ions to ferrous one.

Furthermore, on the XRD pattern and Mössbauer spectrum of sample after treatment at 350 °C, the line of ferrous oxide (Fe_xO) is observed (Fig. 8). Wherein on XRD pattern the reflex linked to ferric stearate vanishes, while two other relatively sharp reflexes located at 2θ angle of 27.3° and 29.9° appear. However, these reflexes also disappear after treatment at 400 °C. We relate these reflexes with the organic residues of ferric(III) stearate decomposition that are crystalline at room temperature. At 350 °C and above, the traces of ferric(III) stearate are not observed both in XRD patterns and Mössbauer spectra. Therefore, as a result of isothermal treatment at 350 °C, ferric(III) stearate is fully decomposed. After treatment at 400 °C and higher temperatures, only magnetite phase is observed.

Processes that are observed in TG-DTG curves from about 350 °C to 500 °C does not reflect in Mössbauer results. These processes are related to the organic residues formed by the pyrolysis/oxidation of ferric(III) stearate. It is known that the common organic products of carboxylate thermal decomposition are ketones and aldehydes [50]. In air atmosphere, these compounds can be further oxidized like the combustion of hydrocarbons. According to the theory of hydrocarbon combustion, these subsequent two processes from about 350–500 °C can be described as fuel deposition (coke formation by pyrolysis and/or oxidative cracking) and high-temperature oxidation (HTO, where coke is combusted), respectively [47,51,52].

For a detailed study of the origin of the doublet associated with ferrous ions, low temperature Mössbauer studies of ferric(III) stearate annealed at 250 °C were carried out. The results are shown in Fig. 9a. The relative area of this component increases strongly with decreasing temperature, which indicates a low Debye temperature. The temperature dependence of the relative area of the component was mathematically least-square fitted using expressions (4) and (6) as shown by a solid red line in Fig. 9b, and the values of the parameters are $\theta_D(0) = 117 \pm 2$ K and $A = -0.166 \pm 0.013$ K^{-1}. The hyperfine parameters are similar to the known values reported in [53] and the low Debye temperature of the component suggests that this doublet is associated with ferrous(II) stearate. Debye temperatures and values of Lamb–Mössbauer factor at room temperature for iron containing phases observed in this work are listed in Table 3. Knowledge of these values is useful for the quantitative analysis of Mössbauer spectra where these phases appear.

Morphology of the obtained samples was analyzed by a high-resolution field emission scanning electron microscope (FESEM). The results for samples calcined at 200 °C, 300 °C, 400 °C, and 500 °C are depicted on Fig. 10. Morphology of samples changes obviously with the rise of calcination temperature, mainly manifested in the surface. For the

sample calcined at 200 °C, it is almost flat surface. But few μm sized flakes are seen on the surface of sample calcined at 300 °C. It may be another proof of the transformation of ferric(III) stearate into ferrous(II) stearate. With the further increasing of calcination temperature, the surface of samples becomes relatively flat. We believe that ~ 1 μm sized roughness on the surface of samples calcined at 400 °C and 500 °C is caused by Fe_3O_4 particles. Apparently, these particles are buried in the residuals of ferric(III) stearate decomposition which are seen on XRD patterns as halo at the 2θ angles of 20°–30° (see Fig. 7). We suppose that these residual products protect magnetite particles from oxidation in the investigated temperature range up to 500 °C and atmosphere pressure.

Obviously, the processes that produce different iron containing phases identified by XRD and Mössbauer spectroscopy from isothermal treatments are consistent with the reaction processes recognized from TG-DTG curves. On the basis of all the obtained results, we assume that the pyrolysis and oxidation of ferric(III) stearate in air atmosphere proceeds along the pathway shown in Scheme 1. The decomposition of ferric(III) stearate at temperatures above 200 °C goes through the formation of an intermediate phase of ferrous(II) stearate. The presence in the reactive medium of iron ions of valence 2+ and 3+ leads to the formation of magnetite particles, i.e. iron oxide of mixed valence. At temperatures of about 300 °C, ferric(III) stearate is completely decomposed, and at about 300–350 °C, ferrous stearate with the formation of iron monoxide (Fe_xO) is observed. At this stage, iron monoxide (Fe_xO) is surrounded by the organic residues (decomposed/oxidized products of organic parts). Further heating leads to the oxidation of Fe_xO to magnetite with the pyrolysis and combustion of organic residues. The two processes visible on the TG-DTG curves at temperatures above 350 °C are associated with fuel deposition (coke formation by pyrolysis and/or oxidative cracking) and HTO of the organic residues.

4. Conclusion

The pyrolysis and oxidation of ferric(III) stearate is a multistage process. At > 200 °C, ferric(III) stearate begins to be decomposed into ferrous stearate. Further heating leads to the formation of a magnetite phase. It should be noticed that three processes can simultaneously occur at 200–300 °C: ferric(III) stearate → ferrous(II) stearate, ferrous(II) stearate → Fe_3O_4, and ferric(III) stearate → Fe_3O_4. When the temperature > 300 °C, ferric(III) stearate is completely decomposed with the formation of iron(II) oxide. Further heating leads to the oxidation of FeO to Fe_3O_4 with the pyrolysis and combustion of organic residues. Fe_3O_4 is the final product of the pyrolysis and oxidation of ferric(III) stearate up to 500 °C. What is noteworthy is that the change in the valence of iron ions is very important for their catalytic effect. These intermediate products and final products can all play a catalytic role in the pyrolysis and oxidation process of hydrocarbons. Insight into the mechanism of the pyrolysis and oxidation process of ferric(III) stearate has a great value for its application as catalysts in in-situ upgrading and combustion for heavy oil recovery as well as in other topics considering iron oxides nanoparticles are one of the most popular catalysts.

CRediT authorship contribution statement

Almaz L. Zinnatullin: Writing – original draft, Investigation, Data curation, Methodology. **Chengdong Yuan**: Methodology, Writing – original draft, Writing – review & editing, Supervision, Project administration. **Dmitrii A. Emelianov**: Investigation, Data curation. **Mikhail A. Varfolomeev:** Conceptualization, Writing – review & editing, Supervision, Project administration. **Farit G. Vagizov:** Conceptualization, Methodology, Investigation, Data curation, Formal analysis, Writing – review & editing.

Declaration of Competing Interest

The authors declare that they have no known competing financial interests or personal relationships that could have appeared to influence the work reported in this paper.

Acknowledgments

References

[1] M. Cheng, C. Lai, Y. Liu, G. Zeng, D. Huang, C. Zhang, L. Qin, L. Hu, C. Zhou, W. Xiong, Metal-organic frameworks for highly efficient heterogeneous Fenton-like catalysis, Coord. Chem. Rev. (2018) 80–92, https://doi.org/10.1016/j.ccr.2018.04.012.

[2] A.M. Kirillov, G.B. Shul'pin, Pyrazinecarboxylic acid and analogs: Highly efficient co-catalysts in the metal-complex-catalyzed oxidation of organic compounds, Coord. Chem. Rev. (2013) 732–754, https://doi.org/10.1016/j.ccr.2012.09.012.

[3] D. Li, X. Ma, Q. Wang, P. Ma, J. Niu, J. Wang, Copper-containing polyoxometalate-based metal-organic frameworks as highly efficient heterogeneous catalysts toward selective oxidation of alkylbenzenes, Inorg. Chem. 58 (2019) 15832–15840, https://doi.org/10.1021/acs.inorgchem.9b02189.

[4] R. Hashemi, N.N. Nassar, P. Pereira Almao, Nanoparticle technology for heavy oil in-situ upgrading and recovery enhancement: opportunities and challenges, Appl. Energy 133 (2014) 374–387, https://doi.org/10.1016/j.apenergy.2014.07.069.

[5] C. Yuan, M.A. Varfolomeev, D.A. Emelianov, M.A. Suwaid, A.A. Khachatrian, V. L. Starshinova, I.R. Vakhitov, A.A. Al-Muntaser, Copper stearate as a catalyst for improving the oxidation performance of heavy oil in in-situ combustion process, Appl. Catal. A Gen. 564 (2018) 79–89, https://doi.org/10.1016/j.apcata.2018.07.021.

[6] C. Yuan, D.A. Emelianov, M.A. Varfolomeev, N.O. Rodionov, M.A. Suwaid, I. R. Vakhitov, Mechanistic and kinetic insight into catalytic oxidation process of heavy oil in in-situ combustion process using copper (II) stearate as oil soluble catalyst, Fuel 284 (2021), 118981, https://doi.org/10.1016/j.fuel.2020.118981.

[7] D.L. Huber, Synthesis, properties, and applications of iron nanoparticles, Small 1 (2005) 482–501, https://doi.org/10.1002/smll.200500006.

[8] D. Faivre, Iron Oxides: From Nature to Applications, John Wiley & Sons, 2016, https://doi.org/10.1002/9783527691395.

[9] E. Paterson, The Iron Oxides. Structure, Properties, Reactions, Occurrences and Uses, John Wiley & Sons, 1999, https://doi.org/10.1180/claymin.1999.034.1.20.

[10] N.L. Ezeonyeka, A. Hemmati-Sarapardeh, M.M. Husein, Asphaltenes adsorption onto metal oxide nanoparticles: a critical evaluation of measurement techniques, Energy Fuels 32 (2018) 2213–2223, https://doi.org/10.1021/acs.energyfuels.7b03693.

[11] N. Hosseinpour, Y. Mortazavi, A. Bahramian, L. Khodatars, A.A. Khodadadi, Enhanced pyrolysis and oxidation of asphaltenes adsorbed onto transition metal oxides nanoparticles towards advanced in-situ combustion EOR processes by nanotechnology, Appl. Catal. A Gen. 477 (2014) 159–171, https://doi.org/10.1016/j.apcata.2014.03.017.

[12] A.R. Brown, A. Hart, V.S. Coker, J.R. Lloyd, J. Wood, Upgrading of heavy oil by dispersed biogenic magnetite catalysts, Fuel 185 (2016) 442–448, https://doi.org/10.1016/j.fuel.2016.08.015.

[13] N.N. Nassar, A. Hassan, P. Pereira-Almao, Metal oxide nanoparticles for asphaltene adsorption and oxidation, Energy Fuels 25 (2011) 1017–1023, https://doi.org/10.1021/ef101230g.

[14] A. Al-Marshed, A. Hart, G. Leeke, M. Greaves, J. Wood, Optimization of heavy oil upgrading using dispersed nanoparticulate iron oxide as a catalyst, Energy Fuels 29 (2015) 6306–6316, https://doi.org/10.1021/acs.energyfuels.5b01451.

[15] M.A. Suwaid, M.A. Varfolomeev, A.A. Al-muntaser, C. Yuan, V.L. Starshinova, A. Zinnatullin, F.G. Vagizov, I.Z. Rakhmatullin, D.A. Emelianov, A.E. Chemodanov, In-situ catalytic upgrading of heavy oil using oil-soluble transition metal-based catalysts, Fuel 281 (2020), 118753, https://doi.org/10.1016/j.fuel.2020.118753.

[16] W. Li, S.S. Lee, J. Wu, C.H. Hinton, J.D. Fortner, Shape and size controlled synthesis of uniform iron oxide nanocrystals through new non-hydrolytic routes, Nanotechnology 27 (2016), 324002, https://doi.org/10.1088/0957-4484/27/32/324002.

[17] R. Hufschmid, H. Arami, R.M. Ferguson, M. Gonzales, E. Teeman, L.N. Brush, N. D. Browning, K.M. Krishnan, Synthesis of phase-pure and monodisperse iron oxide nanoparticles by thermal decomposition, Nanoscale 7 (2015) 11142–11154, https://doi.org/10.1039/c5nr01651g.

[18] M. Unni, A.M. Uhl, S. Savliwala, B.H. Savitzky, R. Dhavalikar, N. Garraud, D. P. Arnold, L.F. Kourkoutis, J.S. Andrew, C. Rinaldi, Thermal decomposition synthesis of iron oxide nanoparticles with diminished magnetic dead layer by controlled addition of oxygen, ACS Nano 11 (2017) 2284–2303, https://doi.org/10.1021/acsnano.7b00609.

[19] W. Baaziz, B.P. Pichon, J.M. Grenèche, S. Begin-Colin, Effect of reaction environment and in situ formation of the precursor on the composition and shape of iron oxide nanoparticles synthesized by the thermal decomposition method, CrystEngComm 20 (2018) 7206–7220, https://doi.org/10.1039/C8CE00875B.

[20] N.N. Song, H.T. Yang, X. Ren, Z.A. Li, Y. Luo, J. Shen, W. Dai, X.Q. Zhang, Z. H. Cheng, Non-monotonic size change of monodisperse Fe3O4 nanoparticles in the scale-up synthesis, Nanoscale 5 (2013) 2804–2810, https://doi.org/10.1039/c3nr33950e.

[21] W. Glasgow, B. Fellows, B. Qi, T. Darroudi, C. Kitchens, L. Ye, T.M. Crawford, O. T. Mefford, Continuous synthesis of iron oxide (Fe3O4) nanoparticles via thermal decomposition, Particuology 26 (2016) 47–53, https://doi.org/10.1016/j.partic.2015.09.011.

[22] Q. Dou, K.M. Ng, Synthesis of various metal stearates and the corresponding monodisperse metal oxide nanoparticles, Powder Technol. 301 (2016) 949–958, https://doi.org/10.1016/j.powtec.2016.07.037.

[23] J. Park, K. An, Y. Hwang, J.E.G. Park, H.J. Noh, J.Y. Kim, J.H. Park, N.M. Hwang, T. Hyeon, Ultra-large-scale syntheses of monodisperse nanocrystals, Nat. Mater. 3 (2004) 891–895, https://doi.org/10.1038/nmat1251.

[24] F. Kenfack, H. Langbein, Synthesis and thermal decomposition of freeze-dried copper-iron formates, Thermochim. Acta. 426 (2005) 61–72, https://doi.org/10.1016/j.tca.2004.07.008.

[25] S.S. Hanna, Chemical applications of Mossbauer spectroscopy, in: V.I. Goldanskii, R.H. Herber (Eds.), Science, 164, Academic Press, New York, 1969, https://doi.org/10.1126/science.164.3882.939.

[26] A. Abras, M.F. De Jesus Filho, M.M. Braga, Mössbauer study of the thermal decomposition of potassium tris(malonato)ferrate(III) trihydrate, Thermochim. Acta. 101 (1986) 35–44, https://doi.org/10.1016/0040-6031(86)80038-7.

[27] P.S. Bassi, B.S. Randhawa, H.S. Jamwal, Mössbauer study of the thermal decomposition of some iron(III) monocarboxylates, Thermochim. Acta. 62 (1983) 209–216, https://doi.org/10.1016/0040-6031(83)85039-4.

[28] K. Muraishi, T. Takano, K. Nagase, N. Tanaka, Thermal decomposition of Fe(II) carboxylates: comparison of decomposition processes between the formate and malonate, J. Inorg. Nucl. Chem. 43 (1981) 2293–2297, https://doi.org/10.1016/0022-1902(81)80252-7.

[29] B.S. Randhawa, R. Kaur, K. Sweety, Mössbauer study on thermal decomposition of some hydroxy iron(III) carboxylates, J. Radioanal. Nucl. Chem. 220 (1997) 271–273, https://doi.org/10.1007/BF02034872.

[30] M.E. Matsnev, V.S. Rusakov, SpectrRelax: an application for Mössbauer spectra modeling and fitting, AIP Conf. Proc (2012) 178–185, 10.1063/1.4759488.

[31] M.A. Varfolomeev, D.K. Nurgaliev, M.V. Kok, Calorimetric study approach for crude oil combustion in the presence of clay as catalyst, Pet. Sci. Technol. 34 (2016) 1624–1630, https://doi.org/10.1080/10916466.2016.1217235.

[32] M.V. Kok, Clay concentration and heating rate effect on crude oil combustion by thermogravimetry, Fuel Process. Technol. 96 (2012) 134–139, https://doi.org/10.1016/j.fuproc.2011.12.029.

[33] M.V. Kök, M.A. Varfolomeev, D.K. Nurgaliev, TGA and DSC investigation of different clay mineral effects on the combustion behavior and kinetics of crude oil from Kazan region, Russia, J. Pet. Sci. Eng. 200 (2021), 108364, https://doi.org/10.1016/j.petrol.2021.108364.

[34] C. Yuan, D.A. Emelianov, M.A. Varfolomeev, Oxidation behavior and kinetics of light, medium, and heavy crude oils characterized by thermogravimetry coupled with Fourier transform infrared spectroscopy, Energy Fuels 32 (2018) 5571–5580, https://doi.org/10.1021/acs.energyfuels.8b00428.

[35] U.I. Leinonen, H.U. Jalonen, P.A. Vihervaara, E.S.U. Laine, Physical and lubrication properties of magnesium stearate, J. Pharm. Sci. 81 (1992) 1194–1198, https://doi.org/10.1002/jps.2600811214.

[36] W. Meisel, P. Tippmann-Krayer, H. Möhwald, P. Gütlich, CEMS/XPS study of iron stearate Langmuir-Blodgett layers, Fresenius J. Anal. Chem. 341 (1991) 289–291, https://doi.org/10.1007/BF00321565.

[37] Y.L. Chen, D.P. Yang, Mössbauer Effect in Lattice Dynamics: Experimental Techniques and Applications, John Wiley & Sons, 2007, https://doi.org/10.1002/9783527611423.

[38] H. Frauenfelder, G.A. Petsko, D. Tsernoglou, Temperature-dependent x-ray diffraction as a probe of protein structural dynamics, Nature 280 (1979) 558–563, https://doi.org/10.1038/280558a0.

[39] K. Burda, A. Hrynkiewicz, H. Kołoczek, J. Stanek, K. Strzałka, Molecular dynamics and local electronic states of Sn and Fe in metallocytochrome and metalloporphyrin, Hyperfine Interact. 91 (1994) 891–897, https://doi.org/10.1007/BF02064624.

[40] G.J. Long, F. Grandjean, T.C. Harrop, H.M. Petroccia, G.C. Papaefthymiou, Combined Mössbauer spectral and density functional study of an eight-coordinate iron(II) complex, Inorg. Chem. 54 (2015) 8415–8422, https://doi.org/10.1021/acs.inorgchem.5b01121.

[41] V.N. Naumov, V.P. Shpakov, I.K. Igumenov, V.R. Belousov, N.A. Nemov, P. A. Stabnikov, G.I. Frolova, V.N. Nogteva, Intermolecular and intramolecular vibrations and their contributions into low-temperature thermodynamics, Chem. Sustain. Dev. B 8 (2000) 237–242.

[42] R. Barbieri. Mössbauer Spectroscopy Applied to Inorganic Chemistry, Springer Science & Business Media, 1986, https://doi.org/10.1016/s0020-1693(00)84597-1.

[43] J.P. Declercq, J. Feneau-Dupont, J. Ladriere, Crystal structure and mössbauer study of tetralithium iron(III) trioxalate chloride nonahydrate, Polyhedron 12 (1993) 1031–1037, https://doi.org/10.1016/S0277-5387(00)87180-6.

[44] G.J. Long, W.T. Robinson, W.P. Tappmeyer, D.L. Bridges, The magnetic, electronic, and Mössbauer spectral properties of several trinuclear iron(III) carboxylate

complexes, J. Chem. Soc. Dalton Trans. (1973) 573–579, https://doi.org/10.1039/DT9730000573.

[45] S. Vyazovkin, K. Chrissafis, M.L. Di Lorenzo, N. Koga, M. Pijolat, B. Roduit, N. Sbirrazzuoli, J.J. Suñol, ICTAC Kinetics Committee recommendations for collecting experimental thermal analysis data for kinetic computations, Thermochim. Acta. 590 (2014) 1–23, https://doi.org/10.1016/j.tca.2014.05.036.

[46] C. Yuan, M.A. Varfolomeev, D.A. Emelianov, A.A. Eskin, R.N. Nagrimanov, M. V. Kok, I.S. Afanasiev, G.D. Fedorchenko, E.V. Kopylova, Oxidation behavior of light crude oil and its SARA fractions characterized by TG and DSC techniques: differences and connections, Energy Fuels 32 (2018) 801–808, https://doi.org/10.1021/acs.energyfuels.7b02377.

[47] C. Yuan, D.A. Emelianov, M.A. Varfolomeev, W. Pu, A.S. Ushakova, Oxidation behavior and kinetics of eight C20-C54n-alkanes by high pressure differential scanning calorimetry (HP-DSC), Energy Fuels 32 (2018) 7933–7942, https://doi.org/10.1021/acs.energyfuels.8b01401.

[48] R. Jasinki, Kinetic parameters from thermal gravimetric data, Nature 201 (1964) 68–69.

[49] S. Vyazovkin, A.K. Burnham, J.M. Criado, L.A. Perez-Maqueda, C. Popescu, N. Sbirrazzuoli, Thermochim. Acta 520 (2011) 1–19.

[50] R. Davis, H.P. Schultz, Studies of thermal decarboxylation of iron carboxylates. I. Preparation of symmetrical aliphatic ketones, J. Org. Chem. 27 (1962) 854–857, https://doi.org/10.1021/jo01050a039.

[51] C. Yuan, D.A. Emelianov, M.A. Varfolomeev, M. Abaas, Comparison of oxidation behavior of linear and branched alkanes, Fuel Process. Technol. 188 (2019) 203–211, https://doi.org/10.1016/j.fuproc.2019.02.025.

[52] C. Yuan, D.A. Emelianov, M.A. Varfolomeev, Oxidation behavior and kinetics of light, medium, and heavy crude oils characterized by thermogravimetry coupled with Fourier transform infrared spectroscopy, Energy Fuels 32 (2018) 5571–5580, https://doi.org/10.1021/acs.energyfuels.8b00428.

[53] N. Saito, T. Tominaga, T. Morimoto, Mössbauer spectroscopic studies of the radiolysis of ferric compounds, Tokyo Univ. (1970), https://doi.org/10.1016/0022-1902(70)80340-2.

[54] E. De Grave, R.E. Vandenberghe, Mössbauer effect study of the spin structure in natural hematites, Phys. Chem. Miner. 17 (1990) 344–352, https://doi.org/10.1007/BF00200130.

[55] G.A. Sawatzky, F. Van Der Woude, A.H. Morrish, Recoilless-fraction ratios for Fe57 in octahedral and tetrahedral sites of a spinel and a garnet, Phys. Rev. 183 (1969) 383–386, https://doi.org/10.1103/PhysRev.183.383.

[56] S. Stølen, R. Glöckner, F. Grønvold, T. Atake, S. Izumisawa, Heat capacity and thermodynamic properties of nearly stoichiometric wüstite from 13 to 450 K, Am. Mineral. 81 (1996) 973–981, https://doi.org/10.2138/am-1996-7-819.